AIAA JOURNAL
Vol. 32, No. 1, January 1994

# Numerical Investigations of Transitional $H_2/N_2$ Jet Diffusion Flames

V. R. Katta* and L. P. Goss†
*Systems Research Laboratories, Inc., Dayton, Ohio 45440*
and
W. M. Roquemore‡
*Wright Laboratory, Wright-Patterson Air Force Base, Ohio 45433*

**A numerical method for accurate simulation of the time and spatial characteristics of the inner and outer vortex structures in transitional $H_2/N_2$ jet diffusion flames is presented. The direct numerical simulation, incorporating buoyancy, a simple one-step chemistry model, and transport coefficients that depend on temperature and species concentration, is described in detail. The species and energy equations are simplified by introducing two conserved scalars $\beta_1$ and $\beta_2$ and by assuming that the Lewis number of the flow is equal to unity. An implicit, third-order-accurate, upwind numerical scheme having very low numerical diffusion is used to simulate the inner small-scale structures and the outer large-scale structures simultaneously. Although the outer structures develop without introducing perturbations, the inner structures are manifested from artificially introduced computer-generated random noise. The buoyancy-driven outer instabilities and the shear-driven inner ones are found to roll up into vortices at frequencies of ~14 and 350 Hz, respectively. Unlike the structures in cold jets, the shear-driven vortices in flames propagate over a long distance without losing their identity or spreading radially. These vortices undergo an unusual axial-growth and merging process that is shown to result from their interactions with the outer vortices. The complex spectral characteristics of the flame are interpreted in terms of the dynamics of this interaction process. The inner vortices appear to have very little impact on the flame since the flame surface is located well outside the jet shear layer.**

## Introduction

THE structural changes that occur in jet diffusion flames during the laminar-to-turbulent transition have been the subject of several studies.[1-7] A typical axisymmetric, transitional jet diffusion flame is illustrated in Fig. 1. The fuel jet emerges from a contoured nozzle having a flat velocity profile at the exit and is surrounded by a low-speed coflowing airstream. Large coherent vortices are observed outside the flame surface, and smaller coherent ones appear inside the flame. The inner vortices develop from a Kelvin-Helmholtz type instability that is amplified by the jet shear layer, similar to the development of the vortex structures in cold jets. However, in cold jets the structures remain coherent for a few jet diameters downstream and then coalesce, which results in the radial growth of the shear layer and the transition to a three-dimensional turbulent flow. This transition sequence is also observed in jet diffusion flames, but the vortices can remain coherent for more than 20 jet diameters downstream before coalescing.[5] During the time that the vortices are coherent, the shear layer does not grow radially. As the vortices coalesce, the shear layer begins to spread radially, the coherence of the inner structures is lost, and a three-dimensional turbulent flow is established. However, the turbulent flame cannot develop until the turbulent fluid interacts with the flame surface. The height in the flame where this occurs is called the break point. At all heights above the break point, the flame surface appears to be highly wrinkled, and the flame is said to be turbulent. The break-point distance decreases with increasing fuel flow rate until either the flame lifts from the nozzle or the entire flame, with the exception of a short region near the nozzle, becomes turbulent. The transition from laminar to turbulent flow occurs at higher velocities in jet flames than in cold jets. A similar transition of the inner structures occurs in jet flames established with fuel tubes; however, the transition process is dependent on the pipe-flow Reynolds number, and the coherent structures are evident only over short distances, as is the case in cold jets.[4,7]

The outer vortex structures shown in Fig. 1 are the dominant characteristic of laminar and transitional jet diffusion flames. Only in the last few years[5,12] has it been realized that these structures are responsible for the much-studied phenomenon referred to by Chamberlin and Rose as "flame flicker."[8] At transitional fuel-jet

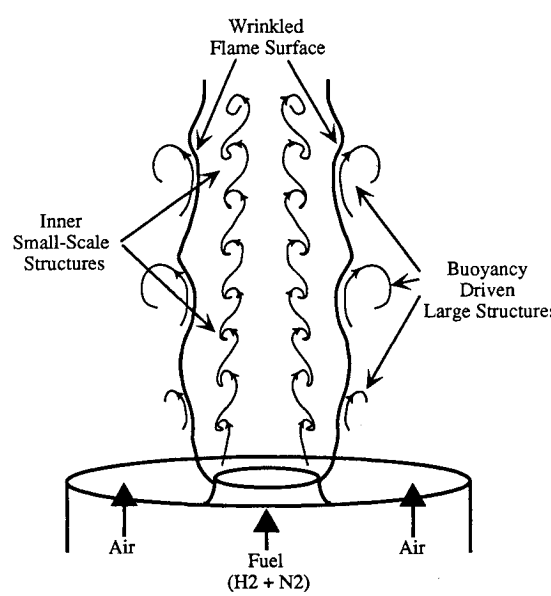


**Fig. 1 Structure of hydrogen jet diffusion flame near transitional fuel-jet velocity and with low coannulus airflow.**

Presented as Paper 92-0335 at the AIAA 30th Aerospace Sciences Meeting, Reno, NV, Jan. 6–9, 1992; received April 11, 1992; revision received May 11, 1993; accepted for publication June 9, 1993. 

*Senior Engineer, Research and Engineering Center, 2800 Indiana Ripple Road. Member AIAA.

†Director of Research, Optical Diagnostics, Research and Engineering Center, 2800 Indiana Ripple Road.

‡Senior Scientist, Fuels and Lubrication Division, Aero Propulsion and Power Directorate. Member AIAA.

velocities, the slowly moving outer toroidal-vortex structures interact strongly with the flame, creating an outward bulge in the flame surface. The flickering appearance of the flame is the result of the upward convective motion of the flame bulge. In the early 1960s, Kimura[9] used linear instability theory to estimate the flame-flicker frequency. Although he obtained a reasonable result, his theory did not explain that this frequency is nearly independent of fuel type, nozzle size, and Reynolds number.[10,11]

Buckmaster and Peters[12] were the first to recognize that buoyancy is responsible for the flow-frequency instability associated with flame flicker. They argued that the natural convection of the flame and the forced convection of the jet are decoupled because the stoichiometric flame surface is located outside the shear layer of the jet, and thus the buoyancy-induced instability is nearly independent of jet characteristics such as fuel exit velocity, nozzle diameter, and fuel type. They performed a linear instability analysis on a two-dimensional infinite candle flame but, unlike Kimura, included buoyancy in the calculation. Their calculation resulted in a flicker frequency that was in good agreement with experiments. An unsatisfactory aspect of their inviscid analysis, however, was that their theory resulted in a flicker frequency that was dependent on streamwise distance to the one-fourth power. Even though this was a weak dependence, it caused a problem in choosing a distance for estimating the flicker frequency that was consistent with the inviscid and large-Reynolds-number assumptions used in their analysis and yet was sufficiently close to the nozzle where the instability was thought to originate. They chose a distance of 3 cm, the approximate location where the outer structures begin to form. Mahalingam et al.[13] questioned the dependence of frequency on streamwise distance. They argued that the instability is present even at the exit of the nozzle where, according to the inviscid analysis, the frequency should be zero. Experimental evidence also indicates that the frequency of the outer instability does not change with streamwise distance within the first 10 nozzle diameters.[14] Buckmaster and Peters recognized the uncertainties associated with the inviscid and parallel-flow assumptions used in their analysis and suggested the formidable task of conducting a detailed viscous analysis of the complete flowfield to examine the points made in their paper.

Recently, direct numerical simulations of buoyant jet flames have provided support and given additional insight into the findings of Buckmaster and Peters and others. By adopting a flame-sheet model, Davis et al.[15] successfully simulated the dynamic structure of a 12-cm/s buoyant propane jet diffusion flame established with a 2.2-cm-diam tube. They showed that the flame is stationary and has no outside vortices when $g = 0$. In the presence of buoyancy, the outer vortex structures develop, and their upward convective motion is shown to be responsible for the 13-Hz flicker frequency associated with the flame bulge. Thus, they confirmed the basic premise of Buckmaster and Peters[12] that buoyancy is the source of flame flicker. Ellzey et al.[16] successfully simulated a transitional hydrogen-nitrogen jet diffusion flame established by a 5-mm contoured nozzle having an exit velocity of 10 m/s. They also showed that the convective motion of the outside vortex structures is responsible for flame flicker and that buoyancy is required to produce these structures. The flicker frequencies computed by Davis et al.[15] and Ellzey et al.[16] were in the range of 11–15 Hz, in agreement with the experimental results. These combined results show that the outer vortex motion and, thus, the flicker frequency, are relatively insensitive to fuel type, Reynolds number, and jet diameter, as demonstrated by experiments.[9–11] This also supports the argument made by Buckmaster and Peters that the buoyancy-induced instability is decoupled from the jet characteristics. However, this point must be examined in flames having inner structures.

The velocity of the flame studied by Ellzey et al. was sufficiently high that one might expect organized inner vortex structures. Although such inner structures did initially form in their calculation, they dissipated rather rapidly due supposedly to volumetric expansion and increased viscosity. Yamashita et al.[17] conducted a numerical study of the laminar-to-turbulent transition in a two-dimensional planar jet diffusion flame in a coflowing airstream. Their results clearly show that the inner structures can interact with the flame and can even produce a low-frequency instability outside the flame surface. However, the impact of this interaction on the outside vortex structures was not studied since buoyancy was not included in their calculations. Recently, Katta and Roquemore performed a numerical study of a transitional propane jet diffusion flame in which the dynamic characteristics of both the inner and the outer vortex structures were captured.[18] Their results suggest that buoyancy—and not viscosity (as suggested by several authors[1,2,5])—is mainly responsible for the long coherence lengths of the inner structures in transitional jet flames. They also showed that small-scale wrinkles occur on the flame surface as a result of the convective motion of the inner vortices but that their overall effect on combustion is small.

In the present paper, the interactions of the outer and inner vortices in a transitional $H_2/N_2$ jet diffusion flame similar to that shown in Fig. 1 are examined. A numerical method for accurately simulating the time and spatial characteristics of the inner and outer vortex structures is described in detail. This method incorporates buoyancy, a simple one-step chemistry model, and transport coefficients that depend on temperature and species concentration. Predictions of the structural features, the mean and fluctuating velocity profiles, and the time-evolving temperature at a fixed axial location compare favorably with experimental results for an $H_2/N_2$ flame having a laminar potential core. The predicted structural features of a transitional $H_2/N_2$ flame having coherent inner structures in the potential core also compare favorably with experimental results. Numerical experiments are used to investigate the source of the inner structures, their growth process, their spectral characteristics, and the influence of the outer structures on these properties.

## Theory

### Mathematical Model

A simple chemistry model is used in which fuel ($H_2$), oxidizer ($O_2$), products ($H_2O$), and inert gas ($N_2$) are assumed to undergo a single global reaction step given as

$$\nu_F \, H_2 + \nu_O \, O_2 + \nu_I \, N_2 \Rightarrow \nu_P \, H_2O + \nu_I \, N_2 \tag{1}$$

The subscripts $F$, $O$, $I$, and $P$ represent fuel, oxidizer, inert gas, and products, respectively, and $\nu$ is the corresponding stoichiometric coefficient. The problem is further simplified by adopting a Shvab-Zel'dovich formulation for the species and energy equations that are written in terms of two scalar variables $\beta_1$ and $\beta_2$, defined as

$$\beta_1 = \frac{\alpha Y_O + Y_F^i - Y_F}{\alpha Y_O^i + Y_F^i} \tag{2}$$

and

$$\beta_2 = \frac{h - h_O^i + (Y_F/\alpha)\, Q}{(Y_F^i/\alpha)\, Q + h_F^i - h_O^i} \tag{3}$$

where $\alpha$ is the fuel-oxidizer ratio ($\nu_F M_F / \nu_O M_O$); $Y_m$ and $h_m$ are the mass fraction and enthalpy of the $m$th species, respectively; $h$ is the mixture enthalpy; $Q$ is the heat release per unit mass of oxygen consumed; $M$ is the molecular weight; and the superscript $i$ represents the initial values. It is assumed that 1) the reaction represented by Eq. (1) occurs at an infinitely fast rate, resulting in an infinitely thin reaction zone or flame sheet, 2) the Lewis number ($Le$ = rate of energy transport/rate of mass transport) is equal to unity, and 3) the Soret and Dufour effects can be neglected. Use of $Le = 1$ with respect to hydrogen flames may not represent the details of the flame structure accurately; however, it is believed that the dynamics of the flames considered in this study are not affected significantly by this assumption. A more recent analysis has also shown that relaxation of this constraint has only negligible

impact on the flame dynamics but significantly increases the computational time.[19]

The time-dependent governing equations written in the cylindrical ($z$, $r$) coordinate system for an axisymmetric reacting flow are

$$\frac{\partial \rho}{\partial t} + \frac{\partial \rho u}{\partial z} + \frac{1}{r}\frac{\partial (r\rho v)}{\partial r} = 0 \tag{4}$$

and

$$\frac{\partial (\rho\Phi)}{\partial t} + \frac{\partial (\rho u\Phi)}{\partial z} + \frac{\partial \rho v\Phi}{\partial r} = \frac{\partial}{\partial z}\left(\Gamma^{\Phi}\frac{\partial \Phi}{\partial z}\right)$$

$$+\frac{\partial}{\partial r}\left(\Gamma^{\Phi}\frac{\partial \Phi}{\partial r}\right) - \frac{\rho v\Phi}{r} + \frac{\Gamma^{\Phi}}{r}\frac{\partial \Phi}{\partial r} + S^{\Phi} \tag{5}$$

where $\rho$ represents density; $u$ and $v$ are the axial and radial components of the velocity vector, respectively; and $p$ is the pressure. The general form of Eq. (5) represents the momentum, species, or energy-conservation equation, depending on the variable used in place of $\Phi$. Table 1 gives the transport coefficients $\Gamma^{\Phi}$ and the source terms $S^{\Phi}$ that appear in the governing equations. Here $\mu$ is the viscosity of the mixture; $D$ is the local binary diffusion coefficient between any two species; $\rho_0$ is the density of air; and $g$ is the gravitational acceleration. The set of equations given by Eqs. (4) and (5) can be completed using the state equation

$$p = \rho T R_0\left(\frac{Y_F}{M_F} + \frac{Y_O}{M_O} + \frac{Y_P}{M_P} + \frac{Y_I}{M_I}\right) \tag{6}$$

where $R_0$ is the universal gas constant; and $T$ is the temperature.

#### Thermodynamic and Transport Properties

The enthalpy of each species is calculated using the polynomial curve fits compiled by Burcat.[20] The mixture enthalpy $h$ is estimated as

$$h = (Y_F h_F + Y_O h_O + Y_P h_P + Y_I h_I) \tag{7}$$

The temperature- and species-dependent transport properties are used in this analysis. First, the viscosity of the individual species is estimated based on the Chapman-Enskog collision theory and then that of the mixture is determined using the Wilke formula.[21] Although four species are involved in the problem, the assumption of infinitely fast chemical reaction will not allow the fuel and oxidizer to be present simultaneously. This means that either $Y_F$ or $Y_O$ should be zero at any time and location and that, at the flame sheet, both vanish. The flame surface can be identified when

$$\beta_1 \equiv \beta_1^* = \frac{Y_F^i}{\alpha Y_O^i + Y_F^i} \tag{8}$$

**Table 1 Coefficients and source terms appearing in governing equations**

| $\Phi$ | $\Gamma^{\Phi}$ | $S^{\Phi}$ |
|---|---|---|
| $u$ | $\mu$ | $-\frac{\partial p}{\partial z} + (\rho_0 - \rho) g + \frac{\partial}{\partial z}\left(\mu\frac{\partial u}{\partial z}\right) + \frac{\partial}{\partial r}\left(\mu\frac{\partial v}{\partial z}\right) + \frac{\mu}{r}\frac{\partial v}{\partial z}$ $-\frac{2}{3}\left[\frac{\partial}{\partial z}\left(\mu\frac{\partial u}{\partial z}\right) + \frac{\partial}{\partial z}\left(\mu\frac{\partial v}{\partial r}\right) + \frac{\partial}{\partial z}\left(\mu\frac{v}{r}\right)\right]$ |
| $v$ | $\mu$ | $-\frac{\partial p}{\partial r} + \frac{\partial}{\partial z}\left(\mu\frac{\partial u}{\partial r}\right) + \frac{\partial}{\partial r}\left(\mu\frac{\partial v}{\partial r}\right) + \frac{\mu}{r}\frac{\partial v}{\partial r} - 2\mu\frac{v}{r^2}$ $-\frac{2}{3}\left[\frac{\partial}{\partial r}\left(\mu\frac{\partial u}{\partial z}\right) + \frac{\partial}{\partial r}\left(\mu\frac{\partial v}{\partial r}\right) + \frac{\partial}{\partial r}\left(\mu\frac{v}{r}\right)\right]$ |
| $\beta_1$ | $\rho D$ | 0 |
| $\beta_2$ | $\rho D$ | 0 |

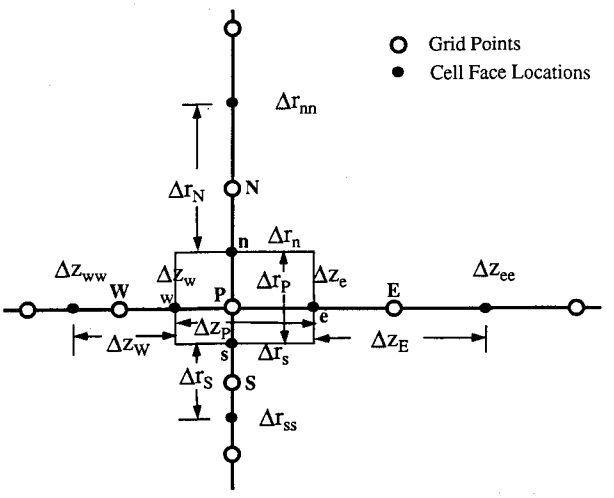


**Fig. 2 Grid spacings and notations used in constructing finite difference scheme.**

The binary diffusion coefficient between any two species is assumed to be identically equal to that of the fuel and nitrogen on the fuel side of the flame and is set identical to that of the oxidizer and nitrogen on the oxidizer side of the flame. The Chapman-Enskog theory and the Lennard-Jones potentials[22] have been used to estimate the previous two binary diffusion coefficients. This approach allows the fuel ($H_2$) and the oxidizer ($O_2$) to diffuse at different rates.

## Numerical Scheme

While studying the cold jet shear layers using the explicit quadratic upstream interpolation for convective kinematics with estimated streaming terms (QUICKEST) scheme,[23] Davis and Moore[24] found that the low numerical diffusion associated with a finite difference scheme is very important in capturing the small-scale structures. Using the same scheme, Davis et al.[15] were also successful in simulating the large-scale buoyancy-driven structures in a jet diffusion flame. The flame investigated in the present study exhibits not only the large-scale buoyancy-driven structures outside the flame sheet but also the shear-driven structures inside the flame that are about the same size as the momentum thickness of the jet. An implicit approach for the QUICKEST scheme has been developed and used successfully to provide a more efficient treatment of the different time scales of the large- and small-scale structures and the source terms that arise from chemical reactions.

A control volume within a staggered grid system and the various distances associated with it are shown in Fig. 2. By adopting the QUICKEST approach for this control volume and calculating the fluxes at the cell faces based on the unknown variable $\Phi$ at the $N+1$th time step, the finite difference form of the scalar equation [Eq. (5)] can be written as follows:

$$A_P\Phi_P^{N+1} + A_{EE}\Phi_{EE}^{N+1} + A_E\Phi_E^{N+1} + A_W\Phi_W^{N+1} + A_{WW}\Phi_{WW}^{N+1}$$
$$+ A_{NN}\Phi_{NN}^{N+1} + A_N\Phi_N^{N+1} + A_S\Phi_S^{N+1} + A_{SS}\Phi_{SS}^{N+1}$$
$$= \Delta t S_p^{\Phi} + \rho_P\Phi_P^N \tag{9}$$

where the superscripts $N$ and $N+1$ represent the known variables at the $N$th time step and the unknown variables at the $N+1$th time step, respectively. The subscripts indicate the location of the variables in Fig. 2. The coefficients in the previous equation are

$$A_{NN} = \frac{\Delta t}{\Delta r_P}\left[-(\rho_n v_n)\Delta r_n^2\left(\tfrac{1}{6} - \gamma_n - \tfrac{1}{6}C_n^2\right)c_1\right]$$

$$A_N = \frac{\Delta t}{\Delta r_P}\left\{(\rho_n v_n)\left[\frac{1}{2} - \frac{C_n}{2} - \Delta r_n^2\left(\tfrac{1}{6} - \gamma_n - \tfrac{1}{6}C_n^2\right)c_2\right]\right.$$

$$+ (\rho_s v_s)\Delta r_s^2\ (^1/_6 - \gamma_s - {}^1/_6 C_s^2)\, d_1 - \frac{\Gamma_n}{r_n}\Bigg\} - \frac{\Delta t}{r_P}\frac{\Gamma_P}{2\Delta r_n}$$

$$A_S = \frac{\Delta t}{\Delta r_P}\Bigg\{-(\rho_n v_n)\Delta r_n^2\ (^1/_6 - \gamma_n - {}^1/_6 C_n^2)\, c_4$$

$$- (\rho_s v_s)\left[\frac{1}{2} + \frac{C_s}{2} - \Delta r_s^2\ (^1/_6 - \gamma_s - {}^1/_6 C_s^2)\, d_3\right] - \frac{\Gamma_s}{\Delta r_s}\Bigg\}$$

$$+ \frac{\Delta t}{r_P}\frac{\Gamma_P}{2\Delta r_s}$$

$$A_{SS} = \frac{\Delta t}{\Delta r_P}\left[(\rho_s v_s)\Delta r_s^2\ (^1/_6 - \gamma_s - {}^1/_6 C_s^2)\, d_4\right]$$

and

$$A_P = \rho_P^N - \{A_{NN} + A_N + A_S + A_{SS} + A_{EE} + A_E + A_W + A_{WW}\}$$

The expressions for $A_{EE}$, $A_E$, $A_W$, and $A_{WW}$ can be written similarly. The local Courant numbers ($C_n$, $C_s$, etc.) and the physical diffusion parameters ($\gamma_n$, $\gamma_s$, etc.) appearing in these coefficients are given by

$$C_n = v_n\frac{\Delta t}{\Delta r_n}, \quad \gamma_n = \Gamma_n\frac{\Delta t}{\Delta r_n^2}, \quad C_s = v_s\frac{\Delta t}{\Delta r_s}$$

$$\gamma_s = \Gamma_s\frac{\Delta t}{\Delta r_s^2}, \qquad \text{etc.}$$

The previous coefficients become functions of the velocity direction as a result of the upwind quadratic differencing that is inherent in the constants $a$, $b$, $c$, and $d$ as follows:

$$v_n \geq 0 \begin{cases} c_1 = 0 \\ c_2 = \left(\dfrac{1}{\Delta r_P}\dfrac{1}{\Delta r_n}\right) \\ c_3 = -\left(\dfrac{1}{\Delta r_P}\dfrac{1}{\Delta r_n} + \dfrac{1}{\Delta r_P}\dfrac{1}{\Delta r_s}\right) \\ c_4 = \left(\dfrac{1}{\Delta r_P}\dfrac{1}{\Delta r_s}\right) \end{cases}$$

$$v_n < 0 \begin{cases} c_1 = \left(\dfrac{1}{\Delta r_N}\dfrac{1}{\Delta r_{nn}}\right) \\ c_2 = -\left(\dfrac{1}{\Delta r_N}\dfrac{1}{\Delta r_{nn}} + \dfrac{1}{\Delta r_N}\dfrac{1}{\Delta r_n}\right) \\ c_3 = \left(\dfrac{1}{\Delta r_N}\dfrac{1}{\Delta r_n}\right) \\ c_4 = 0 \end{cases}$$

$$v_s \geq 0 \begin{cases} d_1 = 0 \\ d_2 = \left(\dfrac{1}{\Delta r_S}\dfrac{1}{\Delta r_s}\right) \\ d_3 = -\left(\dfrac{1}{\Delta r_S}\dfrac{1}{\Delta r_s} + \dfrac{1}{\Delta r_S}\dfrac{1}{\Delta r_{ss}}\right) \\ d_4 = \left(\dfrac{1}{\Delta r_S}\dfrac{1}{\Delta r_{ss}}\right) \end{cases}$$

$$v_s < 0 \begin{cases} d_1 = \left(\dfrac{1}{\Delta r_P}\dfrac{1}{\Delta r_n}\right) \\ d_2 = -\left(\dfrac{1}{\Delta r_P}\dfrac{1}{\Delta r_n} + \dfrac{1}{\Delta r_P}\dfrac{1}{\Delta r_s}\right) \\ d_3 = \left(\dfrac{1}{\Delta r_P}\dfrac{1}{\Delta r_s}\right) \\ d_4 = 0 \end{cases}$$

Expressions can be written in a similar fashion for the other constants.

The previous finite difference scheme [Eq. (9)] is third order accurate both spatially and temporally. Although Eq. (9) is written in the general form of the scalar equation [Eq. (5)], care must be exercised when generating the finite-difference schemes for the $u$ and $v$ momentum equations because of the staggered grid adopted. The four equations represented by Eq. (9) are solved individually using an iterative alternative direction implicit (ADI) technique that involves obtaining solutions for pentadiagonal matrices in the $z$ and $r$ directions iteratively until the residual drops below a specified value. Although these equations are solved independently, a consistent sequence should be followed for simulating time-dependent combusting flows. In the present simulation the equations for $\beta_1$ and $\beta_2$ are solved first, and then the temperature and density at the $N + 1$th time step are obtained. Based on the previous density, the $u$ and $v$ momentum equations are solved next.

**Pressure Solver**

Solution at the $N + 1$th time step is completed by solving the mass continuity equation [Eq. (4)] for pressure. The slowly moving buoyant structures are extremely sensitive to the accuracy of the pressure field. The SIMPLE method[25] for solving the pressure field was used in earlier attempts to simulate the buoyancy-driven structures for an $H_2/N_2$ diffusion flame; these attempts failed, although success was achieved in the case of a propane flame. This iterative pressure solver could not determine the pressure field around the large-scale buoyant structures with sufficient accuracy because of the additional pressure drop that occurred due to the natural buoyant acceleration of the hydrogen. The result was an oscillating flame that did not have the well-defined structures observed in the experiments. The projection method suggested by Chorin[26] was used to circumvent this difficulty. Earlier Peyret and Taylor[27] used this method in simulating the unsteady jet flowing into a stratified fluid, and Davis et al.[15] employed it in simulating buoyant propane flames.

The projection method along with the direct solver used in the present study are described later. At every time step, the $u$ and $v$ momentum equations are solved for $u^*$ and $v^*$, with the assumption that the pressure is uniform everywhere in the flowfield. The actual velocities $u^{N+1}$ and $v^{N+1}$ at this time step can be written as

$$u^{N+1} = u^* + u' \tag{10}$$

$$v^{N+1} = v^* + v' \tag{11}$$

where $u'$ and $v'$ are the errors in the velocity field due to the constant pressure assumption. By substituting Eqs. (10) and (11) into the momentum equations [Eq. (9)], the following relations between the error velocities and the pressure gradients can be obtained:

$$\rho_e^{N+1} u_e' = -\Delta t\left(\frac{p_E^{N+1} - p_P^{N+1}}{\Delta z_P^u}\right) \tag{12}$$

$$\rho_n^{N+1} v_n' = -\Delta t\left(\frac{p_N^{N+1} - p_P^{N+1}}{\Delta r_P^v}\right) \tag{13}$$

where the superscripts $u$ and $v$ to the geometrical parameters indicate the grid sizes used in solving the $u$ and $v$ momentum equations, respectively. Now the pressure Poisson equation is obtained by substituting Eqs. (10–13) into the finite difference form of the continuity equation [Eq. (4)]:

$$\frac{\rho_e^{N+1}u_e' - \rho_w^{N+1}u_w'}{\Delta z_P} + \frac{r_n\rho_n^{N+1}v_n' - r_s\rho_s^{N+1}v_s'}{r_P\Delta r_P}$$

$$= -\left(\frac{\rho_e^{N+1}u_e^* - \rho_w^{N+1}u_w^*}{\Delta z_P} + \frac{r_n\rho_n^{N+1}v_n^* - r_s\rho_s^{N+1}v_s^*}{r_P\Delta r_P}\right)$$

$$= -\dot{m} \tag{14}$$

If Eq. (14) is multiplied by $r_P\Delta r_P\Delta z_P$, the following symmetric-pressure Poisson equation for an orthogonal grid system is obtained:

$$r_P\Delta r_P\left[\left(\frac{p_E^{N+1} - p_P^{N+1}}{\Delta z_e^u}\right) - \left(\frac{p_P^{N+1} - p_W^{N+1}}{\Delta z_w^u}\right)\right]$$

$$+\Delta z_P\left[r_n\left(\frac{p_N^{N+1} - p_P^{N+1}}{\Delta r_n^v}\right) - r_s\left(\frac{p_P^{N+1} - p_S^{N+1}}{\Delta r_s^v}\right)\right]$$

$$= \frac{r_P\Delta z_P\Delta r_P}{\Delta t}\dot{m} \tag{15}$$

The previous equation represents a system of algebraic expressions, with one equation at each grid point. Equation (15) is solved directly using the matrix inversion method in conjunction with the lower and upper (LU) decomposition technique. Finally, the velocities are corrected based on Eqs. (10) and (11), and then the temperature and density are updated.

### Grid System and Boundary Conditions

Since the flowfield associated with a transitional jet diffusion flame can be complicated by the presence of the localized small-scale flow structures within a large domain, careful grid management is required. An orthogonal grid system having rapidly expanding cell sizes in both the $z$ and $r$ directions was used in the present analysis. A typical grid system is shown in Fig. 3. Grid lines are clustered within the shear layer to resolve the small-scale structures, and the boundaries are shifted sufficiently to minimize the propagation of disturbances (which arise due to the inaccuracies in the boundary conditions) in the region of interest. As shown in the figure, most of the grid points in the radial direction are concentrated within the flame zone. The grid spacing in the axial direction is gradually increased to take advantage of the fact that the small-scale structures grow as they are convected downstream. The large outside structures can be accurately captured, even with a coarse grid; hence, no special consideration was given to these structures during construction of the grid system.

The outflow boundary is the most difficult one to treat in these flows because the flow leaving this boundary continuously evolves in time as the large outside and small inside vortices are convected through the boundary. In incompressible and subsonic flows, the flowfield at the outflow boundary cannot be determined solely from the upstream flow conditions. Several procedures[24] are cited in the literature for dealing with outflow boundaries; however, none proved to be adequate for the present calculation because of the passage of structures having different length scales. Thus, a simple extrapolation procedure with weighted zero and first-order terms was used. The main criterion used in selecting the weighting functions was that the vortices crossing this outflow boundary should exit without being distorted. Although this procedure is simple and accurate, some judgment is required on a case-by-case basis.

Calculations are usually initiated with uniform flow conditions everywhere; however, during the first few (< 100) time steps, the simulations are forced for a steady-state solution. This can easily be accomplished by updating the temperature and density immedi-

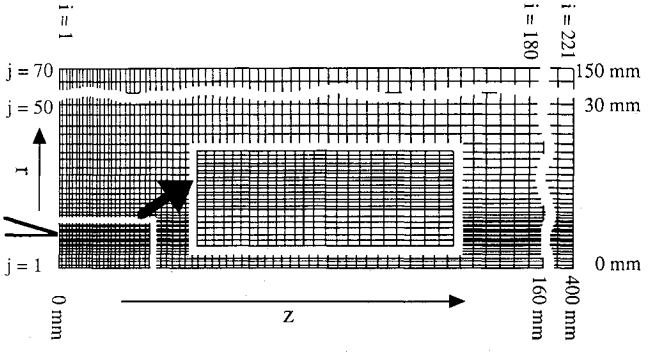


**Fig. 3 Typical grid system used for simulations.**

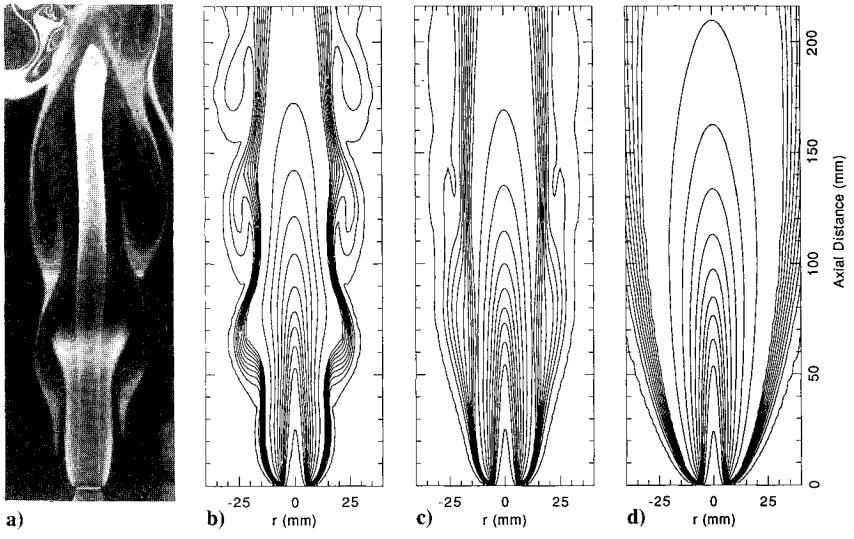


**Fig. 4 Comparison of experimental and computed flames for fuel-jet velocity of 3.26 m/s: a) reactive-Mie-scattering image of experimental flame, b) instantaneous temperature contours of oscillating flame, c) isotemperature contours obtained from averaged flame, and d) isotemperature contours of predicted flame when gravitational force is neglected.**

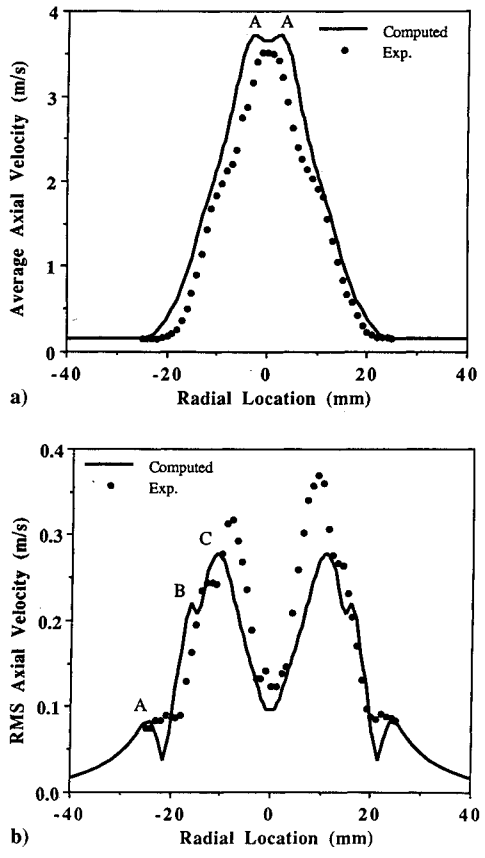


**Fig. 5 Computed and measured axial-velocity distributions in radial direction at height of 40 mm above nozzle: a) average velocities and b) rms velocities.**

ately after solving the $\beta_1$ and $\beta_2$ equations. For a typical calculation, a 221 × 70 grid system is used, and the stable solution is usually obtained in about 5000 time steps, which requires ~50 min of CPU time on a Cray XMP.

## Results And Discussion

Two types of structures can develop in transitional jet diffusion flames: the large-scale vortices outside the flame sheet and the small-scale vortex structures enclosed by the flame sheet. The ability of the numerical model to simulate these outer and inner structures was evaluated for two flames in the present study. The first flame is characterized by the large outside structures and a laminar potential core. The advantage of studying this flame is that the effects of the dynamic motion of the outside structures on the velocity profiles and the time-dependent temperature field can be addressed without concern for the impact of the inner structures. The second flame has both inner and outer structures. The stability characteristics of the inner structures, their interaction with the larger outside structures, and their frequency characteristics were examined.

### Buoyant $H_2/N_2$ Jet Diffusion Flame Having Laminar Potential Core

Extensive experimental studies have been conducted on the buoyant, laminar jet flame chosen for the model-evaluation study.[28–30] The fuel was a mixture of hydrogen and nitrogen in a volumetric ratio of 3.5 to 1. The flame was stabilized on a contoured nozzle having an exit diameter of 10 mm. The fuel jet was mounted vertically and had a mass-averaged exit velocity of 3.26 m/s. The flame was surrounded by a 150-mm-diam coannular air jet having a velocity of 15 cm/s, which helped to shield the central jet flame from room air disturbances. Flow visualizations, mean and rms velocities, and time-dependent temperature data have been collected for this flame. The measured peak flame temperature was ~1900 K. Preliminary calculations under these conditions resulted in an oscillating flame having a flame temperature of ~2600 K. The difference in the calculated and measured temperatures is believed to be due to the lack of radiation and finite rate chemistry models and the use of the unity-Lewis-number assumption in the numerical simulation. More realistic calculated temperatures were obtained by reducing the heat-release parameter [Q in Eq. (3)] by 20%. This lowered the calculated flame temperature to ~2100 K. An instantaneous image of the experimental flame visualized by the reactive-Mie-scattering technique is shown in Fig. 4a.[28] At this low jet velocity, the shear layer is laminar in nature, and shear-layer instabilities have not developed. Two outside large-scale structures are clearly visible, and a portion of a third one at the top is somewhat smeared by the room air.

An instantaneous isotemperature contour plot of the computed flame is shown in Fig. 4b at a phase very near that of the experimental image in Fig. 4a. It should be pointed out that no artificial perturbations were introduced to generate these buoyancy-driven structures. It is not clear how the first vortex is generated; once developed, however, it rolls along the flame surface as it is convected downstream. During this process, the vortex interacts strongly with the flame, making the flame surface bulge and squeeze. This motion is simulated by the time-dependent calculations, as observed in animations of the dynamic characteristics of the flame. Freezing of the flame motion, as in Figs. 4a and 4b, shows that the bulging and squeezing of the experimental and computed flame surfaces occur at about the same heights. It should also be noted that the computed flame has three outer vortices, whereas the experimental image shows only two and one-half vortices. The reduced amount of heat release used in the calculations to compensate for the radiation heat losses accounts for this difference. This reduction lowered not only the peak temperature but also the temperature outside the flame surface. The weaker buoyancy forces associated with the reduced temperature (or higher density) around the computed flame surface reduce the size of the vortical structures, as confirmed by calculations made without modifying the heat-release value. Excellent agreement was obtained between the calculated and measured flame-flicker frequency. At 80 mm above the nozzle, a 12.8-Hz frequency was

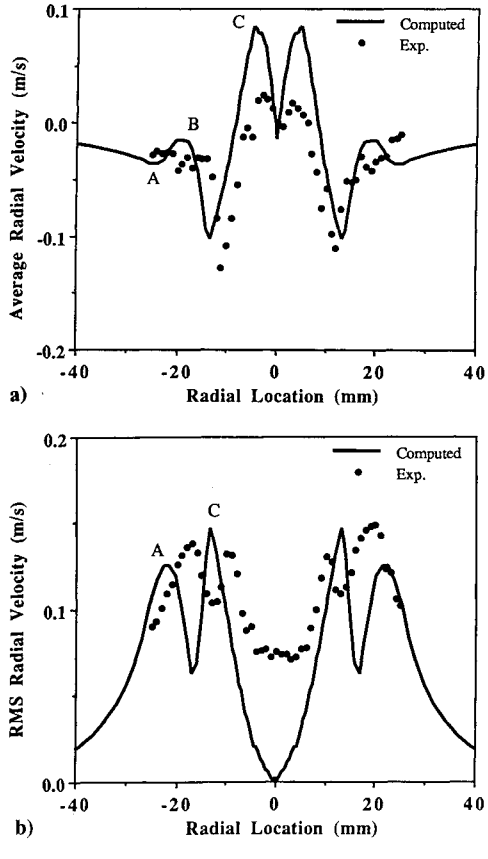


**Fig. 6 Computed and measured radial-velocity distributions in radial direction at height of 40 mm above nozzle: a) average velocities and b) rms velocities.**

obtained from the computed temperature fluctuations, whereas the frequency was observed to be ~13 Hz in the experiments.

The average of several instantaneous temperature contours is plotted in Fig. 4c. In the averaged view, the second and third buoyant structures have disappeared, but the first structure is still evident as a locally diffused flame. Since the mean temperature reflects the time the flame spends in a given location, the presence of the first bulge indicates that the flame spends considerable time in the bulged position at an axial location between 50 and 100 mm. The isotherms in the interior of the jet ($r < 10$ mm) are only moderately affected by the dynamic motion of the outer structures, as evidenced by the similarity of the instantaneous (Fig. 4b) and averaged (Fig. 4c) isotherms.

To illustrate that gravity is an essential factor in generating the outside structures, calculations were also performed with a zero gravitational field. Solution for this case converged to a steady-state flame having a perfectly smooth flame surface. Isotemperature contours in the flow are shown in Fig. 4d. In the middle of the calculation, the flame surface was artificially disturbed to determine whether it would become unsteady. The disturbance was damped, and the flowfield converged to a steady-state solution. Without buoyancy, the flame has no outside structures and is very fat compared with the laboratory flame. The flame diameter at 200 mm above the nozzle in this case is ~70 mm, whereas it is only 20 mm in the experimental flame and 21 mm in the calculated dynamic flame. When the buoyancy terms are activated in Eq. (9), the flame quickly settles into periodic oscillation, with an instantaneous structure similar to that in Fig. 4b. These observations are similar to those of Davis et al.[15] and Ellzey et al.[16] for propane and hydrogen flames, respectively.

Radial profiles of mean and rms values of axial and radial velocities at a height of 40 mm above the nozzle are shown in Figs. 5 and 6. The measured[28,29] values are represented by solid circles and the computed results by lines. It is evident that the simulation correctly predicts the unusual shape of the mean and rms profiles presented. The simulation predicts the change in slope of the profile at 15 and 12 mm in Fig. 5a. Also, it correctly predicts the peaks and valleys in Figs. 5b and Fig. 6. To a great extent, the shape of the profiles is the result of the flame oscillations induced by the convective and rotational motion of the outer vortices. For example, the two peaks in the rms axial velocity denoted by A and B in Fig. 5b appear as a result of the periodic passage of vortices across this section. Since these vortices are convected axially, only one peak appears in the rms radial-velocity profile (A in Fig. 6b). Had the outer vortices been perfectly symmetric about the vortex center, then averaging would have eliminated this peak. The presence of a valley (A) and a peak (B) in Fig. 6a indicates that the structure of the vortex is very complex. The other peaks (C in Figs. 5b and 6b) arise from the radial oscillation of the flame surface. The reasonable predictions of the shape of the profiles indicate that the simulation is capturing the essential dynamic features of the outside vortices and the induced flame oscillations.

The simulation typically overestimates the radial locations of the peaks, inflection points, and other distinguishing features of the mean and rms profiles in Figs. 5 and 6. Also, the magnitude of the peaks is not always correctly predicted. These problems are believed to be due, in part, to the lack of a radiation model and insufficient modeling of the attachment of the flame at the nozzle tip. It is known, and also clear from Fig. 4a, that the hydrogen diffusion flame is anchored a few millimeters upstream of the nozzle exit. This means that the flame surface is outside the shear layer of the jet, even at the nozzle lip. Since the nozzle lip is not considered in the calculations, the calculated flame develops in the shear layer at the nozzle exit; however, it rapidly moves out of the shear layer as the flow progresses downstream. The proximity of the flame to the shear layer at the first few grid points heats up the cold fuel jet and creates an overshoot in the axial velocity at the shear layer due to the gravitational acceleration. This overshoot, which remains up to about 80 mm above the nozzle exit can be seen at the edge of the shear layer in the computed velocity profile at point A in Fig. 5a.

The dynamic temperature characteristics of both the computed and the laboratory flames are compared in Fig. 7. The computed time-evolving isotemperature contours are shown in Fig. 7a as the large outer structures are convected past a fixed radial line 80 mm above the nozzle tip. The data shown at $t = 200$ ms represent the

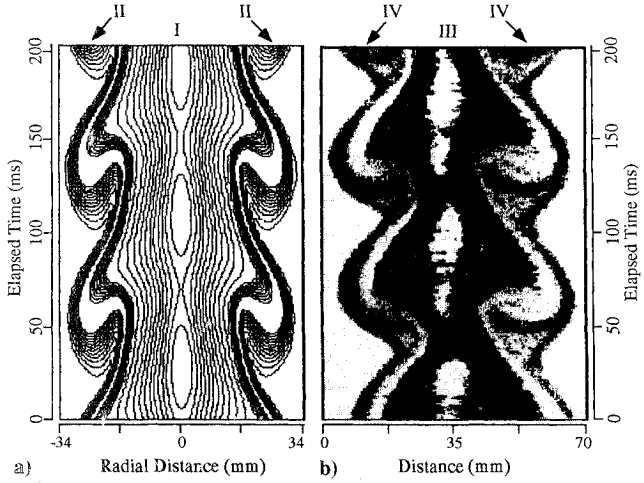


**Fig. 7 Comparison of dynamic behavior of flame at height of 80 mm above nozzle: a) isotemperature contours from calculated data, b) temperature history of experimental flame recorded by thin-filament-pyrometry technique.**

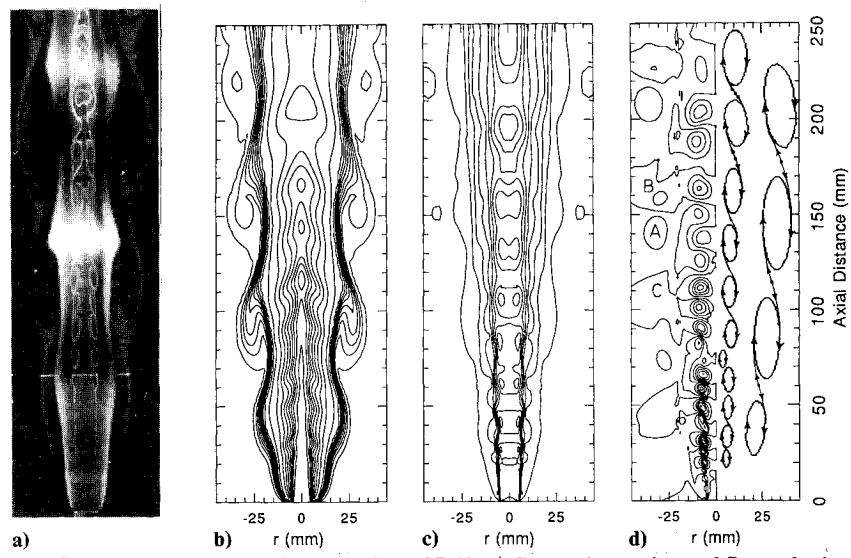


**Fig. 8 Visualization of large-scale outer and small-scale inner vortices of 7.64 m/s flame: a) experimental flame obtained with reactive-Mie-scattering technique, b) instantaneous isotemperature contours of computed flame, c) instantaneous isoaxial velocity map, and d) instantaneous isoradial velocity contours (left side) and speculated vortex structure (right side).**

temperature recorded 200 ms before that shown at 0 ms. Two different contour levels were chosen to highlight the motion of the outer structures and the flame oscillation. In the high-temperature region (I in Fig. 7a), 20 equally spaced contours are plotted between 1500 and 2400 K. The convective motion of the outer vortex is marked (II in Fig. 7a) by the 12 equally spaced contours between 400 and 800 K. Bulging and squeezing of the flame due to the convective motion of the outer vortices cause the periodic oscillation in the flame surface and create the elliptical-shaped islands of relatively cold fuel (<1500 K) near the centerline of the jet. The temperature evolution of the experimental flame at the same height ($z$ = 80 mm) was obtained by the thin-filament-pyrometry[30] technique and is plotted in Fig. 7b; the spatial and temporal scales are those used for plotting the computed results. The data shown in region III of Fig. 7b represent the temperature recorded by the filament that is sensitive to temperatures above 1100 K. The reactive-Mie-scattering data[30] shown in Region IV and the temperature data were obtained simultaneously and are superimposed in Fig. 7b. A comparison of Figs. 7a and 7b shows that the calculations have accurately captured the time-evolving temperature field. However, the computed outer vortex is smaller in Fig. 7a. This is believed to be due to the reduced value of $Q$ in the calculation and the differences in the visualization techniques used in the experiment and calculations. The computed outer vortex is identified from the temperature contours; in the experiment it is identified by illuminating the $TiO_2$ particles trapped inside the vortex. The period of oscillation measured from this plot (~78.8 ms) matches that obtained from the frequency data.

The analysis presented here shows that the numerical simulation predicts the flame structure, mean and rms velocity profiles, and the time-evolving temperature profile reasonably well for the 3.26-m/s jet flame having a laminar potential core. The next test of the model is to determine whether it can be used to simulate a transitional jet flame having both inner and outer structures.

**Buoyant Transitional $H_2/N_2$ Jet Diffusion Flame Having Outer and Inner Structures**

Coherent small-scale structures were experimentally observed when the fuel velocity was increased to 7.64 m/s. The volumetric ratio between the hydrogen and nitrogen in this case was 3.44 to 1. A reactive-Mie-scattering image of an instantaneous flame is shown in Fig. 8a. This flame is highly symmetric, even up to a height of 250 mm (25 diameters) and has well-organized structures both outside and inside the flame surface. As the inner vortices move downstream, they are squeezed radially and elongated axially but still retain their symmetry.

Numerical simulations of this flame were conducted using a flat velocity profile at the nozzle exit. The outside structures appeared shortly after the calculation was initiated and settled into a repetitive pattern. However, the inner shear layer became very laminar in nature, having no structures. Although the outside vortices cause the jet shear layer to oscillate, even at the fuel nozzle exit, this low-frequency disturbance was not amplified in the jet shear layer and, thus, did not stimulate the growth of the small-scale structures. Extensive efforts were made to determine whether changes in grid spacing, time step, and physical properties of the species would cause the inner vortices to appear. These attempts were unsuccessful. In the experiments, both the outer and inner vortices were always present, with no apparent driving of the flow. A review of the literature suggested that the noise that is inevitably present in experiments initiates the instability. This noise was not being taken into account in the simulation.

Gutmark and Ho,[31] in an extensive review of spreading rates and preferred modes in cold jets, pointed out that both the data scatter in reported values of the preferred frequency mode and the spreading rate are larger than expected, based on experimental error. After studying jets in different facilities, they came to the conclusion that the dynamics of a laminar shear layer are controlled by an instability and that the small background perturbations always present in a test facility initiate the instability. They suggested that the development of a shear layer is strongly dependent on the nature of the background perturbations at the nozzle exit. The background noise in the numerical model used to calculate the $H_2/N_2$ flame structure is considerably smaller than that in the experiments. A contoured nozzle was used in the jet flame experiments to generate a flat velocity profile at the nozzle exit having an estimated rms value of ~2.5% of the mean velocity. The spectral characteristics of this fluctuation were not measured. The possibility cannot be ruled out that the fluctuations at the nozzle exit provided the background perturbations needed to stimulate the inner structures in the experiments. Indeed, the work of Gutmark and Ho suggests that this is the case.

In the next attempt to generate the shear-layer instabilities in the calculations, different types of disturbances were introduced at the fuel-jet exit. All led to the development of small-scale structures. To avoid driving the shear layer with perturbations having a frequency or magnitude bias, we used the following procedure for introducing disturbances in subsequent calculations. A few millimeters above the nozzle, but within the shear layer, a circular zone having a radius of three grid spacings was chosen. At all of the grid points within this zone, disturbances were introduced in the axial-velocity component. At every point a random number between −0.5 and +0.5 was generated. The axial velocity at that grid point was then modified as follows:

$$u = u^* (1.0 + 0.01^* \text{ random number}) \qquad (16)$$

This introduced a maximum of 1% unbiased fluctuation in the axial velocity. Velocity fluctuations at every grid point within the selected zone of disturbance were introduced after every time step. Perturbations triggered the instabilities in the calculations; however, sustaining them required sufficient grid spacings and time steps. The former was easily determined by allowing at least seven grids in each direction to lie within the expected vortex. A decision on the time step was made based on trial-and-error calculations. A time step corresponding to a Courant-Friedricks-Levy (CFL) number of 1.0 was used in the final calculations. The CFL number is defined as $\Delta t^* U_{\text{Jet}}/\min(\Delta z_{\min}, \Delta r_{\min})$.

A computed solution of the flame with 1% random noise at the nozzle exit is shown in Fig. 8, along with the experimental image. The phase of the computed and experimental flames has been matched reasonably well. Computed isotherms and axial- and radial-velocity contours are shown in Figs. 8b–d, respectively. In each of the figures, it is evident that the inner vortices are present; however, their features are dependent on the visualization technique employed. In the isotherms, the vortices appear as wavy lines; in the isoaxial velocity contours, they are shown as packets of fluid that appear to be coupled in some way. The inner vortices are more evident in the isoradial-velocity contours of Fig. 8d. Constant radial-velocity contours are plotted in the left half of Fig. 8d; interpretation of these contours in terms of vortex structures is difficult because each vortex is composed of both positive (outward) and negative (inward) radial velocities. For example, point A in Fig. 8d represents a radially inward velocity contour that would be present at the trailing edge of a vortex. Points B and C represent outward velocities that would be at the leading edge of a vortex. Pair B and A would represent one vortex. It is much easier to use color contours to match a pair of isoradial-velocity contours with a vortex. The elliptical-shaped inner and outer structures identified from color contours (not shown in the figure) are displayed in the right half of Fig. 8d.

Streakline plots were also used to highlight the inner and outer vortex structures. These plots can be interpreted more easily than the radial-velocity contours, as shown in Fig. 9 where the streaklines are generated by injecting massless particles at a fixed rate from the fixed spatial locations indicated by open circles. The particles were then visualized in the flowfield at one instant in time. The solid circles in Fig. 9 show the location of the flame surface that was identified from the computed peak temperatures. For entraining particles into the outer vortices, particles were injected along a line near the outer vortex. As expected, the particles injected within the shear layer at the nozzle exit entered the inner vortices and remained there. However, this was not the case with the outer vortices. Each outer vortex continuously entrained new

particles from the annulus airflow as it lost some to the flame zone. The loss of fluid from the outer vortices reduces their growth rate.

A comparison of the calculated flame in Figs. 8 and 9 with the experimental flame in Fig. 8a shows that the simulation provides a good prediction of the structural features of the inner vortices. The numerical model is able to predict the flame surface location with reasonable accuracy up to a location of ~200 mm above the nozzle. For example, the computed flame diameters at the first three flame bulges from the nozzle are 37, 41, and 42 mm, respectively, as compared with 32, 41, and 41 mm measured from the experimental image. Also, the frequency of the computed inner vortices, as noted by the number of vortices per unit length, is about the same as that in the experiments. The simulation also correctly predicts the unusual spatial development of the vortices as they are convected downstream. Note that in the experiment, Fig. 8a, the vortices in the shear layer of the jet do not grow radially as they do in cold jets. Instead, the vortices grow axially and become elongated as they are convected downstream. The computed inner vortices in Figs. 8d and 9 exhibit these same characteristics.

These calculations showed that the development and growth of the inner structures have little impact on the outer structures. However, some secondary effects are present. The inner vortices perturb the temperature field slightly, as evidenced by the small wiggles superimposed on the long-wavelength spatial oscillation in the isotemperature contours near the shear layer in Fig. 8b. No other effects of small-scale structures on large-scale ones were observed. However, the large-scale structures have a major impact on the small-scale ones.

The large-scale structures contribute to a very different type of growth and merging process in the small-scale structures. In Fig. 9 the flame location is marked by the large dots. Note that the inner vortices located where the flame is squeezed are longer than their neighbors. This can be understood in terms of the dynamics of the radial flame oscillations induced by the outer vortices. As the flame is squeezed toward the centerline, the fluid inside it accelerates in much the same way as it would if it were flowing in a flexible tube in which the walls were flexing in and out. The dynamics of the flame oscillation are such that all of the inner vortices that pass locations where the flame is moving inward undergo a local axial stretching or elongation due to the acceleration of the inner fluid. Elongation of the inner fluid also takes place in the absence of inner vortices. The dynamics of this process can be seen in Fig. 7. The elongation process can also result in a head-to-tail type of merging of the inner vortices, as can be observed at a height of ~80 cm in Fig. 9. This merging is very different from that observed in conventional shear layers where the vortices roll around each other and grow radially. The elongation process and the axial merging are also evident from a careful inspection of the visualized flame in Fig. 8a. Similar growth and merging processes are also evident in the propane and methane transitional jet flame visualizations published in Ref. 5. The elongation and axial-merging process has a significant impact on the spectrum of the transitional flame.

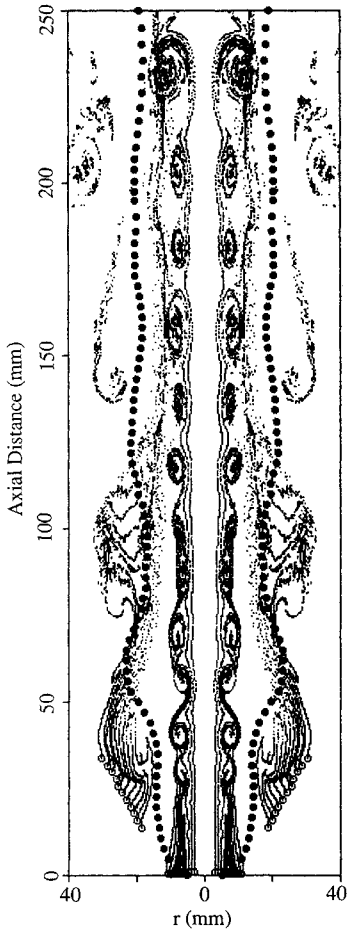


**Fig. 9 Streaklines obtained from particles released at nozzle exit and at locations marked with open circles in annular flow.**

### Calculated Spectrum of Transitional $H_2/N_2$ Flame

Figure 10 shows frequency spectra obtained from temperature data collected at a radial location of 5 mm within the shear-layer at different axial distances from the nozzle exit. The data stored from 10,000 time steps covered a real time of 0.75 s. The calculated spectra compare favorably with those recently measured by Lee in a 10-mm-diameter jet diffusion flame fueled by hydrogen and nitrogen in a mixture ratio of 3.5 to 1 at an exit velocity of 7.8 m/s.[32] Lee used Fourier transforms to obtain the spectrum from time and spatially resolved temperature measurements made using thin filament pyrometry at several heights in the flame. The spectral peaks at a height of 51 mm were compared with those shown in Fig. 10 at a height of 50 mm. The measured peak frequency was ~340 Hz, with smaller peaks at ~380, 480, 300, 240, and 15.6 Hz. This compares favorably with the calculated peak frequency of 350 Hz and smaller peaks at ~380, 420, 300, 260, and 14 Hz. Spectra measured at downstream locations showed the same trends as those in Fig. 10. That is, the peak frequencies decreased with height. A similar shift from high to low frequency with height in the flame was also observed by Yule et al.[1] for a 6-m/s methane flame having well-organized inner vortices. From this limited analysis, the simulation appears to calculate the spectrum reasonably well, which suggests that it has captured the essential physics of the problem.

The high-frequency bands in the spectra in Fig. 10 show the frequency distribution at which the inner vortices are convected past the measurement point in the flame. The distribution of the frequencies is the result of the unusual axial growth and merging process of the inner structures induced by the outer structures. As previously discussed, the inner vortices undergo axial elongation and merging due to oscillations of the flame surface. It should also be noted in Figs. 8a and 9 that the elongation process is not the same for all inner vortices or even neighboring vortices since the inner vortices have different spatial and time histories as they are convected downstream. For example, during one period of the 14-Hz flame oscillation, the number of 1-cm-long inner structures that will pass the measurement point at a fixed height is ~55. Also, in an axial direction, the inner vortices are moving much faster than the outer ones, but not so fast that they would be affected by some radial displacement of the flame during the time it takes them to pass along the length of the flame. The flame is in a slightly different position at the time of formation of each inner vortex. As each vortex is convected downstream, it experiences a slightly different acceleration and deceleration than its neighbor due to the influence of flame oscillation. The result of this process is that vortices have different axial growth rates or lengths. The different frequencies at one axial location in Fig. 10 result from the different lengths and axial velocities of the vortices. The frequencies are bunched relatively close together because the time and spatial history differs only slightly from vortex to vortex. The decrease in frequency with axial distance is a result of the general axial growth of the vortices as they move downstream. The axial growth with downstream dis-

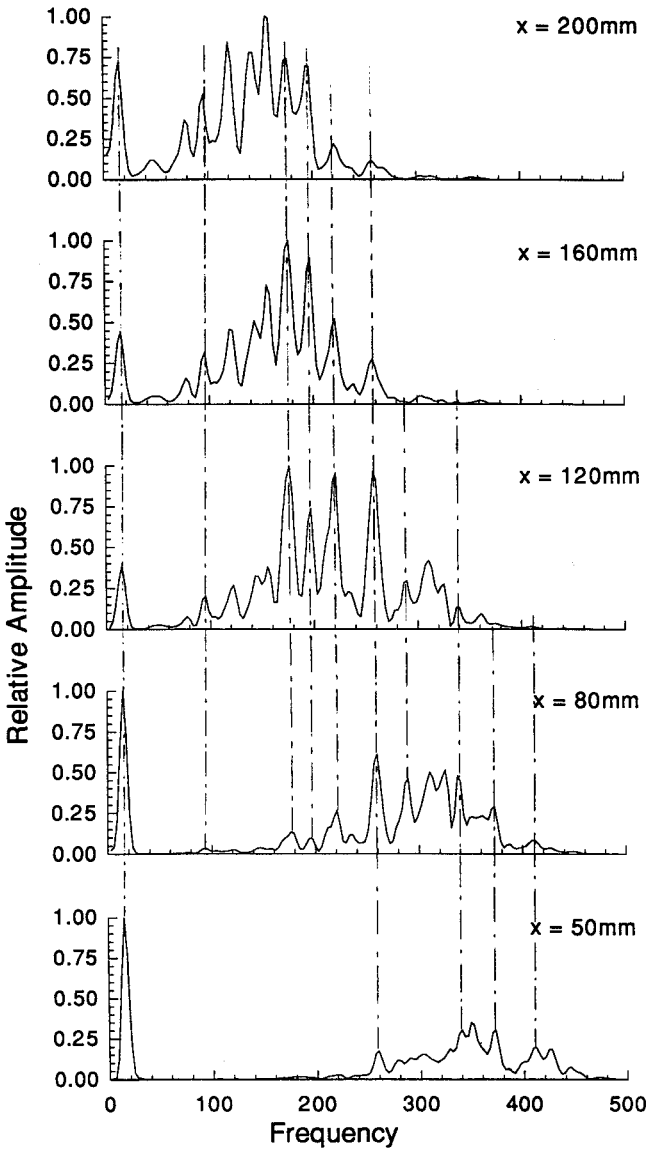


**Fig. 10 Frequency spectra obtained from temperature data recorded within the shear layer at different axial locations.**

tance is due to the repeated elongations and possibly to mergings that occur as the inner vortices pass along the length of the flame. The mergings, however, do not necessarily produce a subharmonic frequency, as noted by inspection of Fig. 10. This is probably due to the complex acceleration experienced by different axial segments of a vortex or merged vortex pair.

The low-frequency component in the spectra in Fig. 10 is the result of the convective motion of the large outside vortex. The computed 14-Hz oscillation of the flame is in reasonable agreement with the 15.6-Hz measured value of Lee in a slightly higher velocity (7.8 m/s as compared with 7.6 m/s) $H_2/N_2$ flame.[32] Note that the lower frequency component remains unaltered at 14 Hz up to a height of 200 mm or 20 jet diameters. That the vortex frequency is independent of axial distance is inconsistent with the results of the linear, inviscid stability analysis of the infinite candle flame performed by Buckmaster and Peters.[12] Their analysis resulted in a frequency dependence of $x^{1/4}$. They also estimated that the frequency of the instability would vary with gravitational constant to the three-fourths power. A recent study[33] by the authors using the simulation described in this paper yielded a frequency dependence of $g^{1/2}$. Furthermore, viscosity was shown to have no effect on the frequency of the outer structures.[33] These discrepancies have raised some concern about the ability of a linear instability analysis to capture the physics of the buoyancy-related instability problem. However, the results of the present paper should resolve any problems concerning the basic assumption made in the analysis by Buckmaster and Peters[12]; this assumption—that the instability associated with the outer structures is essentially decoupled from the forced flow—is correct, even for transitional flames with inner vortex structures. The reason for the decoupling is evident in Fig. 9. The flame surface, established at the location where the fuel and oxygen meet in stoichiometric proportions, lies several millimeters outside the jet shear layer. As the jet velocity increases, the separation between the flame and the jet shear layer decreases and the outer vortex structures weaken as they become an increasing part of the forced flow.

## Summary and Conclusions

A direct numerical method for accurate simulation of the time and spatial characteristics of the inner and outer vortex structures in two transitional $H_2/N_2$ jet diffusion flames has been presented. The numerical method incorporating an implicit, third-order-accurate, upwind scheme with very low numerical diffusion has been described in detail. This method provides direct numerical solutions to the time-dependent conservation equations and incorporates buoyancy, a simple one-step chemistry model, and transport coefficients that depend on temperature and species concentration.

The ability of the numerical model to predict accurately the time-averaged and dynamic characteristics of a low-speed buoyant $H_2/N_2$ jet diffusion flame having a laminar potential core is evaluated. The flame chosen for this evaluation had been extensively studied experimentally. The model correctly predicted the structural features of this flame, including the large vortices outside of the flame surface. The vortices had a measured frequency of 13 Hz, which compared favorably with a calculated frequency of 12.8 Hz. Mean and rms velocity profiles were obtained by averaging instantaneous velocity flowfield calculations over several cycles of the outer structures. Model predictions of the axial and radial velocities and their rms values compared favorably with the experimental results, even revealing the irregular features in the profiles due to the convective motion of the outer vortices. Time-evolving temperature along a radial line eight nozzle diameters downstream also compared favorably with measured data. However, the predicted flame temperature was ~700 K higher than that measured; this is believed to be due to a lack of radiation and finite rate chemistry models in the simulation. To compensate for this temperature difference, the fuel heating value in the calculations was reduced by 20%, which not only lowered the predicted temperature but also reduced the size of the outer structures. When $g$ was set equal to zero in the calculation, the outside structures disappeared and the flame became perfectly laminar, which confirms the findings of others, i.e., that buoyancy is required to form the outside structures.

Constant external forcing in the form of background noise at the exit of the jet was required to initiate and sustain the instabilities that give rise to the inner vortices. This finding is not surprising to the community that studies instabilities, but its importance in both experimental and computational studies is often overlooked. In the presence of buoyancy, the outer structures formed without any intentional application of perturbation to the flow. The instability responsible for the initiation of the outer vortices is felt to be absolutely unstable; thus, only one-time perturbation is required to initiate the oscillation. Such a perturbation can arise from a slight mismatch in the initial, assumed starting solution and the first iterated solution. Once the oscillation begins, it is self-sustaining. This view is currently being examined in some detail.

Predictions of a flame having inner and outer vortices compared favorably with experiments. An examination of the computed and experimental results shows that the growth and merging of the inner vortices are dominated by the motion of the outside structures. The outer vortices cause the flame surface to oscillate. As the inner vortices pass through the contracted and expanded regions of the flame, they become stretched axially (elongated) by the acceleration of the flow, and axial merging can take place. As a result the shear layer experiences very little radial growth. This radial growth and merging process is very different from that in

cold jets and in higher speed jet diffusion flames. The predicted frequency spectra, which compared favorably with the limited experimental results, could be physically interpreted in terms of the axial-growth process of the inner vortices.

## Acknowledgments

This work was supported, in part, by Air Force Contract F33615-90-C-2033. The first author also acknowledges the National Research Council and Air Force Systems Command for sponsoring him on the Postdoctoral Fellowship Program during 1989–91. This research was also supported, in part, by the Aerospace Sciences Directorate of the Air Force Office of Scientific Research. The authors would like to thank Marian Whitaker for her help in preparing the manuscript.

## References

[1]Yule, A. J., Chigier, N. A., Ralph, S., Boulderstone, R., and Ventura, J., "Combustion-Transition Interaction in a Jet Flame," *AIAA Journal,* Vol. 19, No. 6, 1981, pp. 752–760.

[2]Eickhoff, H., and Winandy, A., "Visualization of Vortex Formation in Jet Diffusion Flames," *Combustion and Flame,* Vol. 60, No. 1, 1985, pp. 99–101.

[3]Savas, O., and Gollahalli, S. R., "Flow Structure in Near-Nozzle Region of Gas Jet Flames," *AIAA Journal,* Vol. 2, No. 7, 1986, pp. 1137–1140.

[4]Coats, C. M., and Zhao, H., "Transition and Stability of Turbulent Jet Diffusion Flames," *Twenty-Second Symposium (International) on Combustion,* The Combustion Inst., Pittsburgh, PA, 1988, pp. 685–692.

[5]Roquemore, W. M., Chen, L.-D., Goss, L. P., and Lynn, W. F., "Structure of Jet Diffusion Flames," *Turbulent Reactive Flows,* edited by R. Borghi and S. N. B. Murthy, Vol. 40, Lecture Notes in Engineering, Springer-Verlag, Berlin, Germany, 1989, pp. 49–63.

[6]Cabelli, A., Pearson, I. C., Shepherd, I. C., and Hamilton, N. B., "Fluid Dynamic Structures in Jet Diffusion Flames: Acoustic Effects," *Experimental Heat Transfer, Fluid Mechanics, and Thermodynamics,* First World Conference on Experimental Heat Transfer, Fluid Mechanics, and Thermodynamics (Dubrovnik, Yugoslavia), Elsevier, New York, Sept. 1988, pp. 627–631.

[7]Takahashi, F., Mizomoto, M., and Ikai, S., "Transition from Laminar to Turbulent Free Jet Diffusion Flames," *Combustion and Flame,* Vol. 48, No. 1, 1982, pp. 85–95.

[8]Chamberlin, D. S., and Rose, A., "The Flicker of Luminous Flames," *Industrial and Engineering Chemistry,* Vol. 20, No. 10, 1928, pp. 1013–1016.

[9]Kimura, I., "Stability of Laminar-Jet Flames," *Tenth Symposium (International) on Combustion,* The Combustion Inst., Pittsburgh, PA, 1965, pp. 1295–1300.

[10]Durao, D. F., and Whitelaw, J. H., "Instantaneous Velocity and Temperature Measurements in Oscillating Diffusion Flames," *Proceedings of Royal Society of London, Series A: Mathematical and Physical Sciences,* Vol. 338, No. 1615, 1974, pp. 479–501.

[11]Grant, A. J., and Jones, J. M., "Low Frequency Diffusion Flame Oscillations," *Combustion and Flame,* Vol. 25, No. 2, 1975, pp. 153–160.

[12]Buckmaster, J., and Peters, N., *Twenty-First Symposium (International) on Combustion,* The Combustion Inst., Pittsburgh, PA, 1986, pp. 1829–1836.

[13]Mahalingam, S., Cantwell, B. J., and Ferziger, J. H., "Stability of Low-Speed Reacting Flows," *Physics of Fluids A,* Vol. 3, No. 6, 1991, pp. 1533–1543.

[14]Chen, L.-D., Seaba, J. P., Roquemore, W. M., and Goss, L. P., "Buoyant Diffusion Flames," *Twenty-Second Symposium (International) on Combustion,* The Combustion Inst., Pittsburgh, PA, 1988, pp. 677–684.

[15]Davis, R. W., Moore, E. F., Roquemore, W. M., Chen, L-D., Vilimpoc, V., and Goss, L. P., "Preliminary Results of a Numerical-Experimental Study of the Dynamic Structure of a Buoyant Jet Diffusion Flame," *Combustion and Flame,* Vol. 83, Nos. 3 & 4, 1991, pp. 263–270.

[16]Ellzey, J. L., Laskey, K. J., and Oran, E. S., "Effects of Heat Release and Gravity on an Unsteady Diffusion Flame," *Twenty-Third Symposium (International) on Combustion,* The Combustion Inst., Pittsburgh, PA, 1990, pp. 1635–1640.

[17]Yamashita, H., Kushida, G., and Takeno, T., "A Numerical Study of the Transition of Jet Diffusion Flames," *Proceedings of Royal Society of London, Series A: Mathematical and Physical Sciences,* Vol. 431, No. 1882, 1990, pp. 301–314.

[18]Katta, V. R., and Roquemore, W. M., "Role of Inner and Outer Structures in a Transitional Diffusion Flame," *Combustion and Flame,* Vol. 92, No. 2, 1993, pp. 274–282.

[19]Katta, V. R., Goss, L. P., and Roquemore, W. M., "Effect of Nonunity Lewis Number on the Dynamics of a Hydrogen-Air Jet Diffusion Flame," AIAA Paper 93-0454, Jan. 1993.

[20]Burcat, A., "Thermochemical Data for Combustion Calculations," *Combustion Chemistry,* Springer-Verlag, New York, 1984, pp. 455–473.

[21]Wilke, C. R., "Viscosity Equation for Gas Mixtures," *Journal of Chemical Physics,* Vol. 18, No. 4, 1950, pp. 517–519.

[22]Reid, R. C., Prausnitz, J. M., and Poling, B. E., *The Properties of Gases and Liquids,* McGraw-Hill, New York, 1987, pp. 733, 734.

[23]Leonard, B. P., "A Stable and Accurate Convective Modeling Procedure Based on Quadratic Upstream Interpolation," *Computer Methods in Applied Mechanics and Engineering,* Vol. 19, No. 1, 1979, pp. 59–98.

[24]Davis, R. W., and Moore, E. F., "A Numerical Study of Vortex Shedding from Rectangles," *Journal of Fluid Mechanics,* Vol. 116, March, 1982, pp. 475–506.

[25]Patankar, S. V., *Numerical Heat Transfer and Fluid Flow,* McGraw-Hill, New York, 1980.

[26]Chorin, A. J., "A Numerical Method for Solving Incompressible Viscous Flow Problems," *Journal of Computational Physics,* Vol. 2, No. 1, 1967, pp. 12–26.

[27]Peyret, R., and Taylor, T. D., *Computational Methods for Fluid Flow,* Vol. X, Springer Series in Computational Physics, Springer-Verlag, New York, 1983, pp. 143–215.

[28]Vilimpoc, V., Systems Research Lab., Inc., unpublished data, Dayton, OH, 1988.

[29]Lynn, W. F., Goss, L. P., Chen, T. H., and Trump, D. D., "Two Component Velocity Measurements on an Axially Symmetric H2-N2 Jet Diffusion Flame," *Proceedings of Central States Section Meeting of the Combustion Inst.* (Indianapolis, IN), May 1988 (Paper No. 23).

[30]Vilimpoc, V., and Goss, L. P., "SiC-Based Thin-Filament Pyrometry: Theory and Thermal Properties," *Twenty-Second Symposium (International) on Combustion,* The Combustion Inst., Pittsburgh, PA, 1988, pp. 1907–1914.

[31]Gutmark, E., and Ho, C.-M., "Preferred Modes and the Spreading Rates of Jets," *Physics of Fluids,* Vol. 26, No. 10, 1983, pp. 2932–2938.

[32]Lee, S., "Flow-Flame Interactions of Transitional Nitrogen Diluted Hydrogen Jet Diffusion Flames," Ph.D. Thesis, Univ. of Iowa, Iowa City, IA, Dec. 1992.

[33]Katta, V. R., Goss, L. P., and Roquemore, W. M., "Numerical Investigations on the Dynamic Behavior of a $H_2$-$N_2$ Diffusion Flame Under the Influence of Gravitational Force," AIAA Paper 92-0335, Jan. 1992.